TOMOGRAPHY® RESEARCH ARTICLE

Quantitative Non-Gaussian Intravoxel Incoherent Motion Diffusion-Weighted Imaging Metrics and Surgical Pathology for Stratifying Tumor Aggressiveness in Papillary Thyroid Carcinomas

David Aramburu Núñez[1], Yonggang Lu[2], Ramesh Paudyal[1], Vaios Hatzoglou[4], Andre L. Moreira[3], Jung Hun Oh[1], Hilda E. Stambuk[4], Yousef Mazaheri[1], Mithat Gonen[5], Ronald A. Ghossein[6], Ashok R. Shaha[7], R. Michael Tuttle[8], and Amita Shukla-Dave[1,4]

[1]Department of Medical Physics, Memorial Sloan Kettering Cancer Center, New York, NY; [2]Department of Radiology, Medical College of Wisconsin, Milwaukee, WI; [3]Department of Pathology, NYU Langone Medical Center, New York, NY; Departments of [4]Radiology, [5]Epidemiology and Biostatistics, [6]Pathology, [7]Surgery, and [8]Medicine, Memorial Sloan Kettering Cancer Center, New York, NY

Corresponding Author:
Amita Shukla-Dave, PhD
Memorial Sloan Kettering Cancer Center,
1275 York Avenue, NY, New York 10065;
E-mail: davea@mskcc.org

Key Words: diffusion-weighted imaging, multi b-value, Gaussian and non-Gaussian, papillary thyroid carcinoma, tumor aggressiveness

Abbreviations: Papillary thyroid cancer (PTC), apparent diffusion coefficient (ADC), papillary thyroid carcinoma (PTC), ultrasonography (US), diffusion-weighted imaging (DWI), intravoxel incoherent motion (IVIM), non-Gaussian (NG), repetition time (TR), echo time (TE), echo planar imaging (EPI), regions of interest (ROIs), magnetic resonance imaging (MRI), leave-1-out cross-validation (LOOCV), extrathyroidal extension (ETE), receiver operating characteristic (ROC), area under the ROC curve (AUC)

ABSTRACT

We assessed a priori aggressive features using quantitative diffusion-weighted imaging metrics to preclude an active surveillance management approach in patients with papillary thyroid cancer (PTC) with tumor size 1–2 cm. This prospective study enrolled 24 patients with PTC who underwent pretreatment multi-b-value diffusion-weighted imaging on a GE 3 T magnetic resonance imaging scanner. The apparent diffusion coefficient (ADC) metric was calculated from monoexponential model, and the perfusion fraction (f), diffusion coefficient (D), pseudo-diffusion coefficient (D^*), and diffusion kurtosis coefficient (K) metrics were estimated using the non-Gaussian intravoxel incoherent motion model. Neck ultrasonography examination data were used to calculate tumor size. The receiver operating characteristic curve assessed the discriminative specificity, sensitivity, and accuracy between PTCs with and without features of tumor aggressiveness. Multivariate logistic regression analysis was performed on metrics using a leave-1-out cross-validation method. Tumor aggressiveness was defined by surgical histopathology. Tumors with aggressive features had significantly lower ADC and D values than tumors without tumor-aggressive features ($P < .05$). The absolute relative change was 46% in K metric value between the 2 tumor types. In total, 14 patients were in the critical size range (1–2 cm) measured by ultrasonography, and the ADC and D were significantly different and able to differentiate between the 2 tumor types ($P < .05$). ADC and D can distinguish tumors with aggressive histological features to preclude an active surveillance management approach in patients with PTC with tumors measuring 1–2 cm.

INTRODUCTION

Currently, many clinicians continue to recommend an aggressive initial management approach to all but the patients with the most low-risk papillary thyroid carcinoma (PTC), which usually includes thyroid surgery and radioactive iodine adjuvant therapy (1). Despite this, a more-stratified, risk-adapted initial management approach has been strongly recommended in the recent American Thyroid Association thyroid cancer clinical practice guidelines (2). The recommendations for either a limited thyroid surgery option (thyroid lobectomy without adjuvant therapy) or an active surveillance management approach (serial observation with neck ultrasonography [US] with surgical intervention deferred until documented disease progression) may be less-drastic incremental options for patients with intrathyroidal papillary thyroid cancers thought to be at low risk for disease-specific mortality and recurrence. These treatment options are being offered on the basis of abundance of data showing excellent clinical outcomes following either thyroid lobectomy or active

ISSN 2379-1381 http://dx.doi.org/10.18383/j.tom.2018.00054

surveillance in properly selected low-risk PTC patients with intrathyroidal disease (1-3). Studies have shown that patients with micropapillary carcinomas having small tumors (size, <1 cm) well confined to the thyroid and without presence of extrathyroidal extension and/or lymph node metastases are good candidates for active surveillance (2). The cumulative risk of extrathyroidal extension and lymph node metastases both increased linearly as the primary tumor increases from 1 to 2 cm (4). It is therefore even more important to ensure that these larger thyroid cancers are confined to the thyroid before considering an observation management approach. US alone is an adequate study for selection of those PTCs with smaller tumors (<1 cm) for active surveillance (5-8). However, for those PTCs with larger tumors (>1 cm up to 2 cm), US has suboptimal sensitivity and specificity in the detection of extrathyroidal extension (9, 10) and cannot reliably detect cervical lymph node metastases deep to the intact thyroid gland or in the infraclavicular, retropharyngeal, and parapharyngeal regions (1). Therefore, some experts have suggested that additional imaging methods be used to verify the absence of disease outside the thyroid when considering a conservative management approach in larger tumors.

Quantitative magnetic resonance imaging (qMRI) is a noninvasive technique that provides images of high spatial resolution with excellent tissue contrast. Quantitative diffusion-weighted imaging (DWI) measures the Brownian motion of water molecules in tumor tissue, which is highly reflective of the cellular organization and membrane integrity (11). DWI has shown promise in the detection, staging, prognosis, and monitoring of thyroid cancers (12-19). Quantitative apparent diffusion coefficient (ADC) metric derived from monoexponential modeling of DWI data, under a Gaussian behavior, using ≥2 b-values (ie, diffusion-weighting factor) (11) reflects tumor cellularity. Recently, clinical relevance for ADC has been shown in assessing extrathyroidal extension in discernable intrathyroidal papillary microcarcinomas (tumor size, <1 cm), an aggressive tumor feature that was limited to identification by surgery only (20).

Le Bihan et al. developed the intravoxel incoherent motion (IVIM) model to describe diffusion in the capillary and tissue compartments separately using multiple b value DWI data set (21, 22). IVIM is a biexponential model, which is based on a Gaussian distribution, and it provides estimates of pseudo-diffusion coefficient (D^*), perfusion fraction (f) within the capillary network, and true diffusion coefficient of the tissue (D) metrics (22). Recent studies have shown the utility of IVIM-DWI in clinical oncology (23-31).

Diffusion in biological tissue is hindered and complex and therefore lends itself well to a non-Gaussian (NG) nature, which has been readily observable via noninvasive imaging at high b-values (32, 33). Using multi-b-value DWI data, NG models [ie, diffusional kurtosis (34, 35) and extension of biexponential IVIM with kurtosis, called NG-IVIM (22, 36)] have been developed to account for hindered and restricted diffusion in tumor tissue. The dimensionless imaging metric K characterizes NG diffusion behavior in tissue microstructure. The quantitative metric K obtained from both diffusion kurtosis and NG-IVIM models has shown feasibility to quantify tissue microstructure in head and neck (HN) cancer (35, 36). Given the known microstructural complexity in PTC, we hypothesized that the NG-IVIM may have greater utility than Gaussian models in risk stratification for active surveillance candidates. The purpose of this study was to identify a priori aggressive histological features using NG-IVIM to preclude an active surveillance management approach in patients with PTC, with tumor diameter size 1–2 cm as measured by US.

MATERIALS AND METHODS

Patients

This clinical study was approved by our institutional review board, which was compliant with the Health Insurance Portability and Accountability Act. In total, 24 patients (age, 27–78 years; male/female, 8/16) were enrolled in this prospective clinical trial, before surgery. All patients who underwent the study signed a form of written consent.

DWI Data Acquisition

MRI examinations were performed on a 3-Tesla GE scanner (General Electric, Milwaukee, WI), with a neurovascular phased-array coil and consisted of standard multiplanar (sagittal, axial, coronal) T1- and T2-weighted imaging scans followed by multi-b-value DWI scans. The T1- and T2-weighted MRI scans covered the whole thyroid gland with a field of view (FOV) of 20–24 cm, slice thickness of 5 mm, and acquisition matrix of 256 × 256. The repetition time (TR)/echo time (TE) for T1-weighted scans were 500 milliseconds (ms)/15 ms; and TR/TE for T2-weighted scans were 4000 ms/80 ms.

Multi-b-value DWI images were acquired using a single-shot spin-echo echo planar imaging (SS-SE-EPI) sequence with TR = 4000 ms, TE = minimum (100–110 ms), number of excitations (NEX) = 4, slice thickness = 5 mm, gap = 0 mm, field of view = 20–24 cm, acquisition matrix of 128 × 128, which was zero-filled and reconstructed to 256 × 256 pixels, with 10 b values of 0, 20, 50, 80, 200, 300, 500, 800, 1000, and 1500 s/mm^2. Images were acquired using 3 orthogonal diffusion gradient direction. The acquisition minimum TE varied between patients (minimum TE 100–110 ms) because of slight differences in obliquity of the prescription. A calibration scan was performed before multi-b-value acquisition to reduce Nyquist (N/2) ghosting artifacts (20, 37). Fat suppression, shimming, and parallel imaging (acceleration factor = 2) techniques were used to reduce imaging artifacts.

DWI Data Processing

The regions of interest (ROIs) on thyroid glands for the PTCs were drawn on the DWI images (b = 0 s/mm^2) by an experienced neuroradiologist (>10 years' experience) using ImageJ (38), in conjunction with the radiological, clinical, and pathological information. All ROIs avoid obvious cystic, hemorrhagic, or calcified portions. All data analyses were performed using an in-house-developed software package, MRI-QAMPER (Quantitative Analysis Multi-Parametric Evaluation Routines) implemented in MATLAB (The MathWorks, Natick, MA). Metric values were estimated on a voxel-by-voxel basis to generate parametric maps, and ROI-averaged values for each quantitative imaging metric were calculated.

The voxel-wise apparent diffusion coefficient (ADC) map within the ROI was calculated from the multi-b-value DWI data, using a monoexponential model given by:

$$S_b = S_0 e^{-b\,ADC} \quad (1)$$

where S_b and S_O are signal intensities with and without diffusion weighting, and b is the diffusion-weighting factor (s/mm^2).

The quantitative imaging metrics estimated from NG-IVIM using the multi-b-value DW-MRI data are given by the following equation (21, 36):

$$S_b = S_0\left[f e^{-bD^*} + (1-f)e^{-bD+\frac{1}{6}Kb^2D^2}\right] \quad (2)$$

where f is the vascular volume fraction; D is the diffusion coefficient (mm^2/s); D^* is the pseudo-diffusion coefficient (mm^2/s) associated with blood perfusion, and K is the diffusion kurtosis coefficient. Under the assumption of a Gaussian distribution ($K = 0$), equation (2) is equivalent to IVIM model equation (21).

Because multi-b-value DWI images are inherently noisy owing to thermal or physiological factors, a noise-rectified method was used for metric estimation, as detailed elsewhere (36). For image processing, DWI data were fitted using a nonlinear least-square fitting method using MRI-QAMPER (24, 36).

Histopathological Examination

Surgical papillary thyroid tumor specimens after radical thyroidectomy or lobectomy were collected under the supervision of an experienced (>10 years) pathologist. Paraffin-embedded tissue blocks were obtained for each surgically resected tumor specimen and stained with hematoxylin and eosin. The hematoxylin and eosin section of each papillary thyroid tumor was reviewed by the same excising pathologist, using established criteria for evaluating tumor aggressiveness (39, 40). The histopathological characteristics of tumor aggressiveness were evaluated individually using the following 6 features: tall cell variant, necrosis, vascular and/or tumor capsular invasion, extrathyroidal extension, regional metastases, and distant metastases. A tumor identified with the presence of any 1 of these features was considered to be aggressive.

US Examination

US examinations were performed according to a standard protocol that includes grayscale and color Doppler US assessment of the thyroid bed and cervical lymph nodes in all neck compartments. US reports include information about size, location, and structure of thyroid nodules and cervical lymph nodes. Size was defined as the largest diameter among the 3 dimensions observed. The US studies were performed with Siemens Acuson S2000 or SEQUOIA (Siemens Medical Solutions, Mountain View, CA), or the GE Logiq 9 (GE Healthcare, Little Chalfont, UK) units, using 8- to 15-MHz linear transducers.

Statistical Analysis

Quantitative imaging metrics ADC, D, f, D^*, and K from NG-IVIM analysis and US measurement values were reported as ROI-based mean ± standard deviation (SD). To compare metric value differences among groups of PTCs with and without features of aggressiveness, a nonparametric Wilcoxon rank-sum test was used. A Spearman correlation analysis was performed between quantitative imaging metrics. The significance level was set at $P \leq .05$.

Finally, the relative percentage change (rc, %) in imaging metrics mean values were calculated as:

$$rc(\%) = \frac{(X_{ag} - X_{nag})}{X_{nag}} \times 100 \quad (3)$$

where X_{ag} and X_{nag} are the quantitative imaging metrics mean values (ie, ADC, D, f, D^* and K) of tumors with and without aggressive features, respectively.

Receiver operating characteristic (ROC) curve analysis was performed for each metric to assess its capability to discriminate between PTC groups with and without aggressive features, resulting in area under the ROC curve (AUC) evaluation. Youdon's index was used to estimate the optimal cutoff values for individual metrics (41, 42). Multivariate logistic regression analysis was performed on relevant metrics using a leave-one-out cross-validation (LOOCV) method for unbiased assessment of the modeling.

All statistical analyses were performed using R software and Stata (43, 44).

RESULTS

Patient characteristics are summarized in Table 1. Of the 24 patients, 13 patients were found to have locoregional metastases by preoperative US imaging. Based on surgical pathology analysis, all 24 patients had PTCs, including 6 patients with the tall cell variant, 1 patient with vascular and/or capsular invasion, 9 patients with extrathyroidal extension, and 16 patients with locoregional metastases. The mean size of the lesion based on US was 16 ± 6 mm and ranged from 6–26 mm.

Figure 1 shows a representative plot of signal intensity decay curve as a function of the b-values (s/mm^2) obtained from a patient with aggressive feature of extrathyroidal extension (ETE) confirmed at surgical pathology.

Figures 2 and 3 show NG-IVIM metric maps overlaid on the DWI images from a representative patient with PTC with aggressive tumor features (female; 28 years; US tumor maximum diameter, 2.1 cm) and a representative patient with PTC without aggressive tumor features (female; 48 years; US tumor maximum diameter, 2.1 cm), respectively. It is interesting to note that maximum tumor diameter in preoperative US was the same for both tumors shown in Figures 2 and 3. However, at surgical pathology, the tumor with aggressive features was found to be in the size range of >2 cm (Figure 2), while tumor with nonaggressive feature was in the size range of 1–2 cm (Figure 3).

Tumors with aggressive features (tall cell variant, necrosis, vascular and/or tumor capsular invasion, ETE, regional metastases, or distant metastases) had significantly lower ADC and D values and higher f values than tumors without aggressive features ($P < .05$) (Figure 2), whereas K and D^* values were not significantly different ($P > .05$) for the 2 groups (Table 2).

Out of the 24 patients, 14 patients were in the critical size range (1–2 cm), and ADC and D were significantly different (Table 2), differentiating between tumors with (n = 10) versus without (n = 4) aggressive features ($P < .05$). The ADC values

Table 1. Patient Characteristics

Characteristic	Values
Age at diagnosis (years)	41 ± 7 (range, 27–78)
Sex	
Female	16 (67%)
Male	8 (33%)
Fine-needle aspiration cytology	
Papillary thyroid cancer	16 (67%)
Suspicious for papillary thyroid cancer	8 (33%)
Preoperative US	
Subcapsular location of tumor	19 (79%)
Extrathyroidal Extension	2 (8%)
Evidence of Lymph node metastases	13 (54%)
Size of papillary carcinoma (mm)	16 ± 6 (range, 6–26)
Histology	
Classic papillary thyroid cancer (cPTC)	13 (54%)
Follicular variant papillary thyroid cancer (fvPTC)	3 (12%)
Diffuse sclerosing PTC (dsPTC)	1 (4%)
Tall cell variant PTC (tPTC)	4 (16%)
Multifocal (cPTC+fvPTC; cPTC+tPTC)	1 + 2 (12%)
Size of papillary carcinoma (mm)	15 ± 6 (range, 5–25)
Aggressive features based on pathology	
Tall cell	6 (25%)
Extrathyroidal extension	9 (38%)
Necrosis	0 (0%)
Vascular and/or tumor capsular invasion	1 (4%)
Regional metastases	16 (67%)
Distant metastases	0 (0%)
Pathology T	
T1a	2 (8%)
T1b	10 (42%)
T2	3 (13%)
T3	9 (38%)
Pathology N	
N0	8 (33%)
N1a	6 (25%)
N1b	10 (42%)
Clinical M	
M0	24 (100%)
M1	0 (0%)
AJCC Stage	
I	17 (71%)
II	2 (8%)
III	3 (13%)
IVA	2 (8%)

were $1.3 \pm 0.3 \times 10^{-3}$ mm^2/s vs $1.9 \pm 0.5 \times 10^{-3}$ mm^2/s for tumors with and without aggressive features, respectively. The D values were $1.3 \pm 0.3 \times 10^{-3}$ mm^2/s vs $2.1 \pm 0.6 \times 10^{-3}$ mm^2/s for tumors with and without aggressive features, respectively. The K, D^*, and f metrics were not significantly different in this cohort ($P > .05$).

Figure 4 boxplot compares the quantitative imaging metrics mean values for ADC, D, and US-measured tumor size (mm) between tumors with and without aggressive features. The absolute relative percentage change (rc, %) in the quantitative imaging metric ADC, D, K, D^*, and f metric values for tumors with aggressive features were 31%, 40%, 46%, 7%, and 31% respectively, in comparison to tumors without aggressive features.

Figure 5 displays the scatter plot between NG-IVIM estimates of two quantitative imaging metrics D and K. The Spearman rank-order correlation coefficient (ρ) was -0.46 ($P < .05$), indicating a significant correlation between the D and K.

Figure 6A shows the estimated ROC curves for quantitative imaging metrics ADC, D, and K. Using ROC analysis, the best cutoff values of ADC, D, and K that discriminate between aggressive PTCs with and without aggressive features were determined as follows: ADC = 1.79×10^{-3} mm^2/s, $D = 1.35 \times 10^{-3}$, and $K = 0.68$. The sensitivity, specificity, and AUC obtained from the ROC curve were 100%, 75%, and 0.875, respectively, for ADC; 80%, 100%, and 0.95, respectively, for D; and 70%, 75%, and 0.725, respectively, for K. The AUC is the highest for metric D, followed by metrics ADC and K. Figure 6B resulted from logistic regression on combined 2 metrics (ADC and D) and 3 metrics which included K based on the LOOCV method. Sensitivity, specificity, and AUC obtained from the LOOCV analysis combining 2 and 3 metrics were as follows: 90%, 75% and 0.70 and 80%, 75%, and 0.65, respectively.

DISCUSSION

To the best of our knowledge there are no published studies that have leveraged the use of biexponential NG-IVIM modeling using multi-b-value DWI data sets to stratify PTCs into tumor groups with and without aggressive features. The quantitative imaging metrics ADC, D, and K exhibit promise as surrogate biomarkers for aggressiveness in patients with PTC, following appropriate validation.

Previously, Lu et al. using monoexponential modeling of quantitative DWI data stratified PTCs into tumor groups with and without ETE, one of the multiple aggressive features, thereby obtaining significantly lower mean ADC values for tumors with ETEs than without $(1.53 \pm 0.25) \times 10^{-3}$ [mm^2/s] vs $(2.4 \pm 0.7) \times 10^{-3}$ [mm^2/s] (20). Previously ETE was identified by surgery only (8, 45). Hao et al., also using DWI, stratified PTCs with and without ETEs, thereby showing significant lower median ADC values for tumor with ETE features $(1.41 \pm 0.29) \times 10^{-3}$ [mm^2/s] vs $(1.53 \pm 0.29) \times 10^{-3}$ [mm^2/s] (46). In the present study the cut-off value of ADC to discriminate PTCs with and without aggressive features was 1.79×10^{-3} mm^2/s and is consistent with the previous studies by Lu et al. and Hao et al., 1.85×10^{-3} mm^2/s and 1.89×10^{-3} mm^2/s, respectively (20, 46).

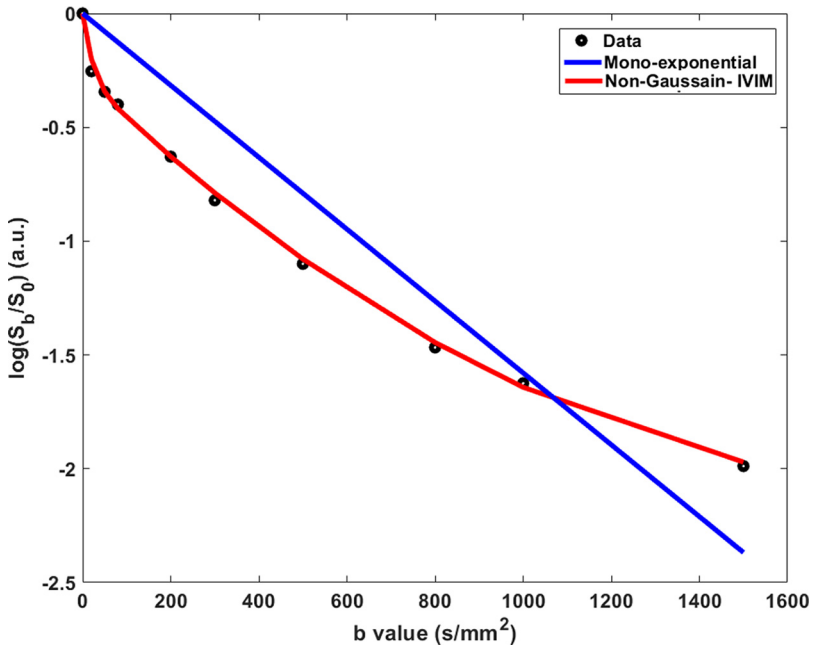

Figure 1. Logarithmic signal intensity (S_b/S_0) plotted as a function of b-value. The experimental data (black circle) obtained from a representative thyroid patient is fitted with a mono exponential model (blue line) and non-Gaussian intravoxel incoherent motion model (red line).

Recently biexponential modeling (IVIM) analysis using multi-b-value DWI data have shown clinical utility in several cancers, including prostate and head and neck (30, 47-49). Valerio et al. have shown that ADC and *D* values are significantly lower in prostate cancer tissue compared with healthy tissue ($0.76 \pm 0.27 \times 10^{-3}$ [mm^2/s] vs $0.99 \pm 0.38 \times 10^{-3}$ [mm^2/s]) (47). In addition, Barbieri et al. found that ADC and *D* differ significantly between high- and low-grade prostate cancer lesions ($0.76 \pm 0.27 \times 10^{-3}$ [mm^2/s] vs $0.99 \pm 0.38 \times 10^{-3}$ [mm^2/s]) (48). The clinical utility of multi-b-value DWI is being tested in cancers in the head and neck region, including the thyroid gland (30, 31, 49). Shen et al. investigated the feasibility of using IVIM to detect radiation changes of normal-appearing parotid glands in patients with differentiated thyroid cancer after radioiodine therapy (49). In a small study of 8 healthy volunteers, Becker et al. used an IVIM-derived imaging metric to

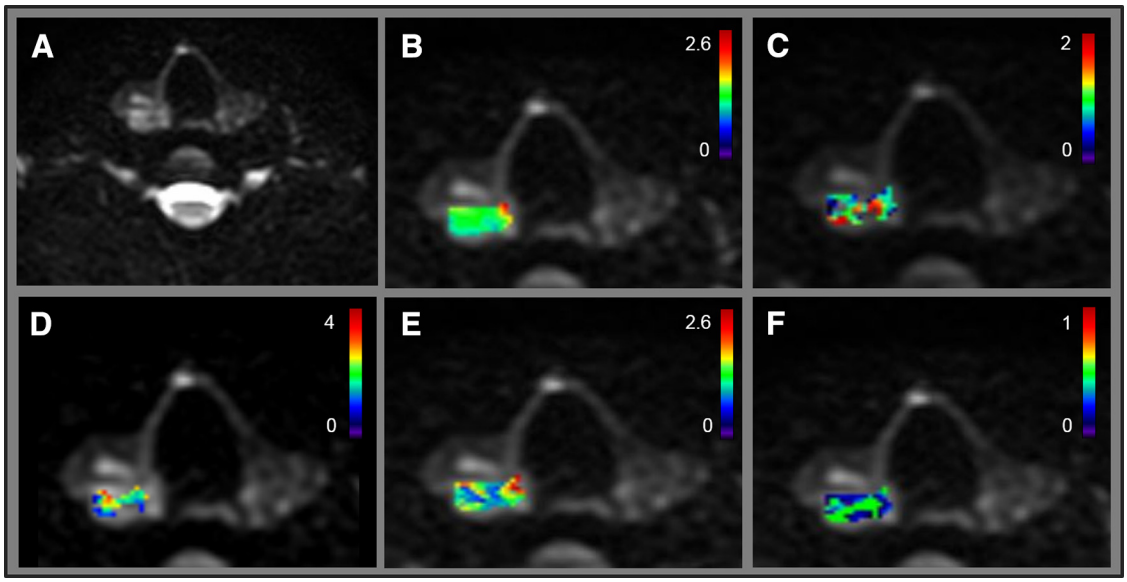

Figure 2. The representative patient with papillary thyroid carcinoma (PTC) with tumor aggressive features (female; 28 years; ultrasonography [US] maximum tumor diameter, 2.1 cm). Diffusion-weighted image (b = 0 s/mm²) (A). ADC map ($\times 10^{-3}$ mm^2/s) overlaid on diffusion-weighted image (b = 0 s/mm²) (B). *K* map overlaid on diffusion-weighted image (b = 0 s/mm²) (C). *D** ($\times 10^{-3}$ mm^2/s) map overlaid on diffusion-weighted image (b = 0 s/mm²) (D). *D* map ($\times 10^{-3}$ mm^2/s) overlaid on diffusion-weighted image (b = 0 s/mm²) (E). *f* map overlaid on diffusion-weighted image (b = 0 s/mm²) (F).

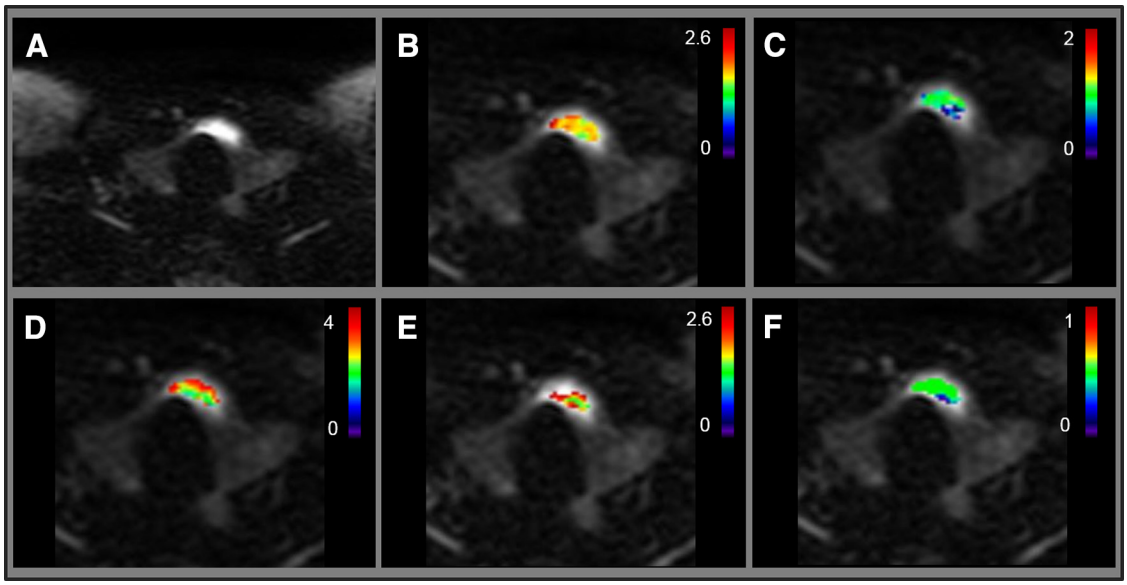

Figure 3. The representative patient with PTC without tumor-aggressive features (female; 48 years; US maximum tumor diameter, 2.1 cm). Diffusion-weighted image (b = 0 s/mm^2) (A). ADC map ($\times 10^{-3}$ mm^2/s) overlaid on diffusion-weighted image (b = 0 s/mm^2) (B). *K* map overlaid on diffusion-weighted image (b = 0 s/mm^2) (C). *D** ($\times 10^{-3}$ mm^2/s) map overlaid on diffusion-weighted image (b = 0 s/mm^2) (D). *D* map ($\times 10^{-3}$ mm^2/s) overlaid on diffusion-weighted image (b = 0 s/mm^2) (E). *f* map overlaid on diffusion-weighted image (b = 0 s/mm^2) (F).

establish a comprehensive description of tissue properties of healthy thyroid tissue (50). The IVIM imaging metric *D* was shown to be significantly different between complete responders (the change between pre- and intratreatment week 3 was from $0.67 \pm 0.17 \times 10^{-3}$ mm^2/s to $0.98 \pm 0.28 \times 10^{-3}$ mm^2/s) and noncomplete responders (the change between pre- and intratreatment week 3 was from $0.59 \pm 0.10 \times 10^{-3}$ mm^2/s to $0.72 \pm 0.03 \times 10^{-3}$ mm^2/s) in patients with head and neck squamous cell carcinoma treated with radiotherapy (31). For tumors with hindered and restricted diffusion, NG-IVIM modeling analysis from multi-b-value DWI, as developed by Lu et al., has shown to be a better-fitting model in head and neck region (36). This model is used in the present study for the first time in the thyroid region.

The findings from 14 patients with PTC with tumor diameter 1–2 cm (as measured by US) emphasize the role of NG-IVIM DWI in differentiating this sub group. Preoperative US could identify 6 out of 14 patients with aggressive features, while NG-IVIM DWI indicated 11 patients. As ground truth, there were 10 patients with aggressive tumor features determined by pathology, our reference standard (Table 2). Therefore, NG-IVIM could correctly identify all 10 patients with aggressive tumor features confirmed by pathology, whereas US correctly identified only 6 patients. US is the

Table 2. Statistical Analysis (mean ± SD) for Quantitative Imaging Metrics Using Tumor Size by US

US Tumor Size	<1 cm (n = 3)		1–2 cm (n = 14)		>2 cm (n = 7)	
Aggressive features on US	YES (n = 2)	NO (n = 1)	YES (n = 6)	NO (n = 8)	YES (n = 5)	NO (n = 2)
Aggressive features on pathology	YES (n = 3)	NO (n = 0)	YES (n = 10)	NO (n = 4)	YES (n = 5)	NO (n = 2)
ADC $\times 10^{-3}$ (mm^2/s)	(1.2 ± 0.7)	–	(1.32 ± 0.27)[a]	(1.9 ± 0.5)[a]	(1.7 ± 0.4)	(2.03 ± 0.06)
D $\times 10^{-3}$ (mm^2/s)	(1.4 ± 0.7)	–	(1.27 ± 0.25)[a]	(2.1 ± 0.6)[a]	(1.7± 0.6)	(2.20 ± 0.08)
*D** $\times 10^{-3}$ (mm^2/s)	(2.61 ± 0.62)	–	(2.84 ± 0.06)	(2.95 ± 0.06)	(2.7 ± 0.3)	(2.98 ± 0.02)
f	(0.17 ± 0.05)	–	(0.21 ± 0.06)	(0.16 ± 0.05)	(0.18 ± 0.05)	(0.10 ± 0.02)
K	(0.7 ± 0.6)	–	(0.70 ± 0.26)	(0.48 ± 0.29)	(0.71 ± 0.28)	(0.64 ± 0.15)

[a]statistical significance $P < 0.05$.

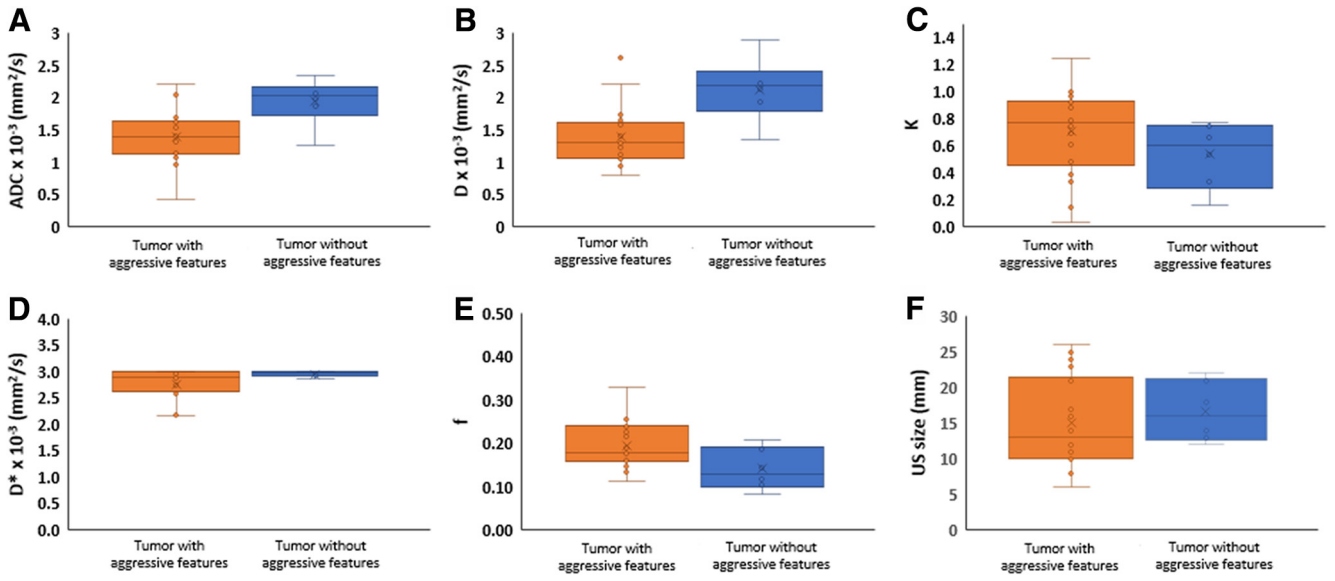

Figure 4. Box-and-whisker plots comparing the mean values for quantitative imaging metrics for all tumors in the 2 groups (tumor with and without aggressive features): ADC × 10^{-3} (mm^2/s) (A), $D \times 10^{-3}$ (mm^2/s) (B), f (C), $D^* \times 10^{-3}$ (mm^2/s) (D), K (E), and radiological information from US (mm) (F).

imaging modality most commonly used to identify and monitor locoregional disease progression and recurrence in thyroid cancer. However, US is unable to preoperatively identify features such as tall cell variant, necrosis, vascular, and/or tumor capsular invasion or distant metastases (5). NG-IVIM DWI were able to correlate nonaggressive tumor features in 3 out of 4 patients, whereas US overestimated nonaggressiveness in 8 patients. These data strongly suggest that US and MRI are complementary and should be used in combination for patients with tumor size in the range of 1–2 cm. This finding is of key clinical importance for treating physicians who are considering active surveillance for said patient population.

Quantitative NG-IVIM DWI and its derived diffusion and perfusion imaging biomarkers have shown promise in this study of patients with PTC when grouped on the basis of different tumors sizes from preoperative US measurements. In addition, for US-measured tumors sized in the range of 1–2 cm, substantial difference was observed in rc (%) in the NG-IVIM-derived metrics between the 2 groups. D is the true diffusion coefficient metric and a surrogate biomarker of tumor cellularity with 40% change, while metric K is considered as an index of tissue microstructure related to hindered and restricted diffusion with 46% change observed for tumors with aggressive features on comparison to tumors without aggressive feature. The rc (%) for imaging metrics f and D^* were 31% and 7%, and these imaging metrics remain exploratory in nature as their biological meaning has yet to be fully understood. In the present study, K was not necessarily independent of D for all tumors but a weak correlation coefficient between these 2 quantitative imaging

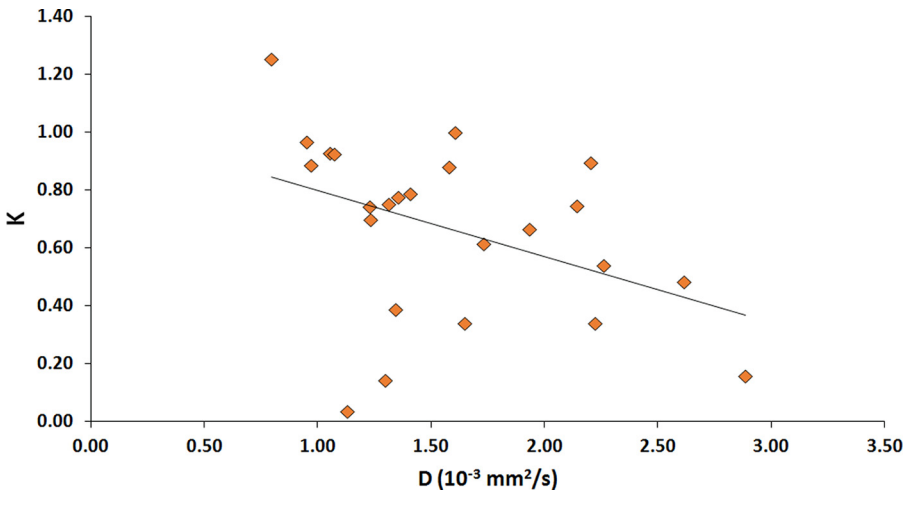

Figure 5. Scatter plot of the true diffusion coefficient (D) and the kurtosis value (K) obtained from all thyroid patients, showing a statistically significant negative correlation ($\rho = -0.46$; $P < 0.05$).

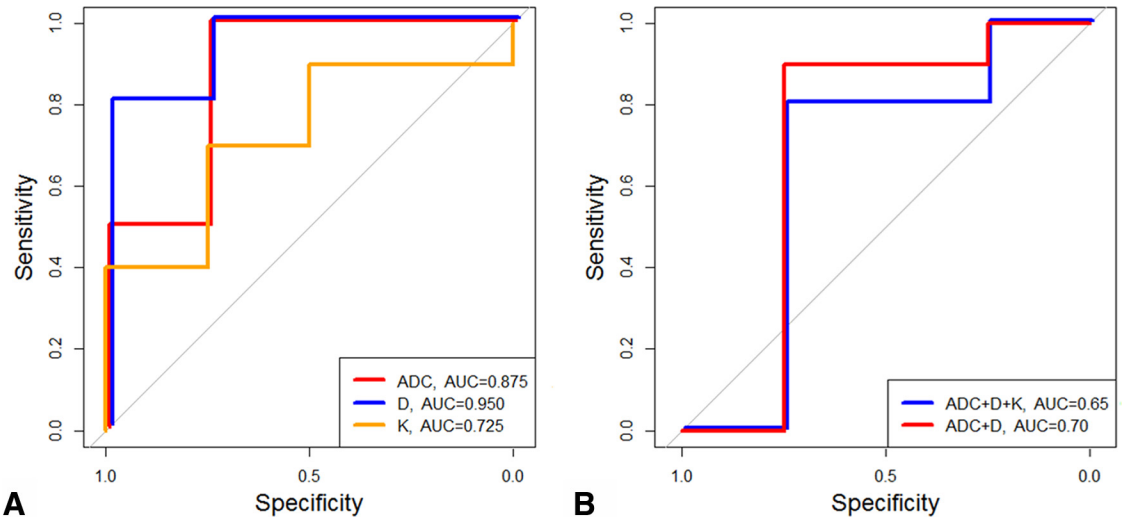

Figure 6. Receiver operating characteristic (ROC) curve to discriminate patients with PTC with and without aggressive features using apparent diffusion coefficient (ADC, black line), *D* (blue line), *K* (orange line) (A). ROC curve from logistic regression based on a leave-one-out cross validation method for the combination of ADC, *D*, and *K* (blue line) and ADC and D (red line) (B).

metrics suggested that *K* might provide additional information related to tissue microstructure. Similar results have been reported previously using NG analysis of DWI in head and neck squamous cell carcinoma (51).

In the present study, for all US-based tumor sizes, the univariate analysis showed the most favorable predictive power with *D* (AUC = 0.95). However, the AUC is lower for both combinations of the metrics in the cross-validation–multivariate analysis, implying cross-validation is necessary to build the predictive model for more realistic and unbiased assessment. The decrease in AUC between 2- and 3- metric models, is due to the metric *K* which may have discriminatory power for US-based tumor size, in the range of 1–2 cm only. For differentiation between the 2 PTC groups, the 2-metric model appears to be the model of choice.

These findings indicate that the quantitative imaging metrics derived from NG-IVIM modeling can provide important risk stratification information and additional insights into potential tumor behavior that cannot be gained from US evaluation alone. As consideration is being given to extend active surveillance to tumors larger than 1 cm, it is increasingly important to develop additional noninvasive tools to help clinicians risk-stratify these slightly larger tumors.

There are several known limitations in this study. First, further investigation is needed in those cohorts with tumors diameters >2 cm and <1 cm. Although no active surveillance is needed for tumors that are >2 cm, it is important to identify aggressive features in tumors that are <1 cm, as has been shown by Lu et al. for papillary microcarcinomas with ETE features (20). Second, a validation study with a larger cohort of patients with PTC is necessary to confirm our initial findings for use in clinical trials. Finally, DWI acquisition using SS EPI suffers from susceptibility artifacts owing to voluntary and involuntary bulk motion in the thyroid region (52). Modified sequences, such as reduced field of view, can help obtain images with fewer distortions (53).

In conclusion, quantitative imaging biomarkers (ADC, *D*, and *K*) derived from NG-IVIM DWI could be used to noninvasively identify tumors with aggressive histological features to preclude an active surveillance management approach in patients with PTC with primary tumor diameters ranging between 1–2 cm.

ACKNOWLEDGMENTS

We would like to thank Mr. Christian Czmielewski (MSc) for his kind contribution to data management and Ms. Eve LoCastro (MS) for carefully editing the manuscript. This research was supported by the National Cancer Institute/National Institutes of Health (grant numbers R21CA176660-01A1 and P50 CA172012-01A1) and in part through the NIH/NCI Cancer Center Support Grant (P30 CA008748).

Disclosures: No disclosures to report.

Conflict of Interest: The authors have no conflict of interest to declare.

REFERENCES

1. American Thyroid Association (ATA) Guidelines Taskforce on Thyroid Nodules and Differentiated Thyroid Cancer; Cooper DS, Doherty GM, Haugen BR, Kloos RT, Lee SL, Mandel SJ, Mazzaferri EL, McIver B, Pacini F, Schlumberger M, Sherman SI, Steward DL, Tuttle RM. Revised American thyroid association management guidelines for patients with thyroid nodules and differentiated thyroid cancer. Thyroid. 2009;19:1167–1214.
2. Haugen BR, Alexander EK, Bible KC, Doherty GM, Mandel SJ, Nikiforov YE, Pacini F, Randolph GW, Sawka AM, Schlumberger M, Schuff KG, Sherman SI, Sosa JA, Steward DL, Tuttle RM, Wartofsky L. 2015 American thyroid association management guidelines for adult patients with thyroid nodules and differentiated thyroid cancer: the American thyroid association guidelines task force on thyroid nodules and differentiated thyroid cancer. Thyroid. 2016;26:1–133.
3. Eggener SE, Mueller A, Berglund RK, Ayyathurai R, Soloway C, Soloway MS, Abouassaly R, Klein EA, Jones SJ, Zappavigna C, Goldenberg L, Scardino PT, Eastham JA, Guillonneau B. A multi-institutional evaluation of active surveillance for low risk prostate cancer. J Urol. 2009;181:1635–1641; discussion 1641.
4. Machens A, Holzhausen HJ, Dralle H. The prognostic value of primary tumor size in papillary and follicular thyroid carcinoma—a comparative analysis. Cancer. 2005;103:2269–2273.
5. Ito Y, Amino N, Miyauchi A. Thyroid ultrasonography. World J Surg. 2010;34: 1171–1180.
6. Ito Y, Masuoka H, Fukushima M, Inoue H, Kihara M, Tomoda C, Higashiyama T, Takamura Y, Kobayashi K, Miya A, Miyauchi A. Excellent prognosis of patients with solitary T1N0M0 papillary thyroid carcinoma who underwent thyroidectomy and elective lymph node dissection without radioiodine therapy. World J Surg. 2010;34:1285–1290.
7. Ito Y, Miyauchi A. Appropriate treatment for asymptomatic papillary microcarcinoma of the thyroid. Expert Opin Pharmacother. 2007;8:3205–3215.
8. Ito Y, Miyauchi A, Inoue H, Fukushima M, Kihara M, Higashiyama T, Tomoda C, Takamura Y, Kobayashi K, Miya A. An observational trial for papillary thyroid microcarcinoma in Japanese patients. World J Surg. 2010;34:28–35.
9. Lee CY, Kim SJ, Ko KR, Chung KW, Lee JH. Predictive factors for extrathyroidal extension of papillary thyroid carcinoma based on preoperative sonography. J Ultras Med. 2014;33:231–238.
10. Gweon HM, Son EJ, Youk JH, Kim JA, Park CS. Preoperative assessment of extrathyroidal extension of papillary thyroid carcinoma comparison of 2- and 3-dimensional sonography. J Ultras Med. 2014;33:819–825.
11. Basser PJ, Jones DK. Diffusion-tensor MRI: theory, experimental design and data analysis—a technical review. NMR Biomed. 2002;15:456–467.
12. Tezuka M, Murata Y, Ishida R, Ohashi I, Hirata Y, Shibuya H. MR imaging of the thyroid: correlation between apparent diffusion coefficient and thyroid gland scintigraphy. J Magn Reson Imaging. 2003;17:163–169.
13. Tunca F, Giles Y, Salmaslioglu A, Poyanli A, Yilmazbayhan D, Terzioglu T, Tezelman S. The preoperative exclusion of thyroid carcinoma in multinodular goiter: Dynamic contrast-enhanced magnetic resonance imaging versus ultrasonography-guided fine-needle aspiration biopsy. Surgery. 2007;142:992–1002; discussion e1–e2.
14. Razek AA, Sadek AG, Kombar OR, Elmahdy TE, Nada N. Role of apparent diffusion coefficient values in differentiation between malignant and benign solitary thyroid nodules. AJNR Am J Neuroradiol. 2008;29:563–568.
15. Schueller-Weidekamm C, Kaserer K, Schueller G, Scheuba C, Ringl H, Weber M, Czerny C, Herneth AM. Can quantitative diffusion-weighted MR imaging differentiate benign and malignant cold thyroid nodules? Initial results in 25 patients. AJNR Am J Neuroradiol. 2009;30:417–422.
16. Bozgeyik Z, Coskun S, Dagli AF, Ozkan Y, Sahpaz F, Ogur E. Diffusion-weighted MR imaging of thyroid nodules. Neuroradiology. 2009;51:193–198.
17. Erdem G, Erdem T, Muammer H, Mutlu DY, Firat AK, Sahin I, Alkan A. Diffusion-weighted images differentiate benign from malignant thyroid nodules. J Magn Reson Imaging. 2010;31:94–100.
18. Schueller-Weidekamm C, Schueller G, Kaserer K, Scheuba C, Ringl H, Weber M, Czerny C, Herneth AM. Diagnostic value of sonography, ultrasound-guided fine-needle aspiration cytology, and diffusion-weighted MRI in the characterization of cold thyroid nodules. Eur J Radiol. 2010;73:538–544.
19. Mutlu H, Sivrioglu AK, Sonmez G, Velioglu M, Sildiroglu HO, Basekim CC, Kizilkaya E. Role of apparent diffusion coefficient values and diffusion-weighted magnetic resonance imaging in differentiation between benign and malignant thyroid nodules. Clin Imaging. 2012;36:1–7.
20. Lu Y, Moreira AL, Hatzoglou V, Stambuk HE, Gonen M, Mazaheri Y, Deasy JO, Shaha AR, Tuttle RM, Shukla-Dave A. Using diffusion-weighted MRI to predict aggressive histological features in papillary thyroid carcinoma: a novel tool for preoperative risk stratification in thyroid cancer. Thyroid. 2015;25:672–680.
21. Le Bihan D. Intravoxel incoherent motion imaging using steady-state free precession. Magn Reson Med. 1988;7:346–351.
22. Le Bihan D, Breton E, Lallemand D, Aubin ML, Vignaud J, Laval-Jeantet M. Separation of diffusion and perfusion in intravoxel incoherent motion MR imaging. Radiology. 1988;168:497–505.
23. Lemke A, Laun FB, Klauss M, Re TJ, Simon D, Delorme S, Schad LR, Stieltjes B. Differentiation of pancreas carcinoma from healthy pancreatic tissue using multiple b-values: comparison of apparent diffusion coefficient and intravoxel incoherent motion derived parameters. Invest Radiol. 2009;44:769–775.
24. Lu Y, Jansen JF, Stambuk HE, Gupta G, Lee N, Gonen M, Moreira A, Mazaheri Y, Patel SG, Deasy JO, Shah JP, Shukla-Dave A. Comparing primary tumors and metastatic nodes in head and neck cancer using intravoxel incoherent motion imaging: a preliminary experience. J Comput Assist Tomogr. 2013;37:346–352.
25. Riches SF, Hawtin K, Charles-Edwards EM, de Souza NM. Diffusion-weighted imaging of the prostate and rectal wall: comparison of biexponential and monoexponential modelled diffusion and associated perfusion coefficients. NMR Biomed. 2009;22:318–325.
26. Sigmund EE, Cho GY, Kim S, Finn M, Moccaldi M, Jensen JH, Sodickson DK, Goldberg JD, Formenti S, Moy L. Intravoxel incoherent motion imaging of tumor microenvironment in locally advanced breast cancer. Magn Reson Med. 2011; 65:1437–1447.
27. Zhu L, Wang H, Zhu L, Meng J, Xu Y, Liu B, Chen W, He J, Zhou Z, Yang X. Predictive and prognostic value of intravoxel incoherent motion (IVIM) MR imaging in patients with advanced cervical cancers undergoing concurrent chemo-radiotherapy. Sci Rep. 2017;7:11635.
28. Lu W, Jing H, Ju-Mei Z, Shao-Lin N, Fang C, Xiao-Ping Y, Qiang L, Su-Yu Z, Ying G. Intravoxel incoherent motion diffusion-weighted imaging for discriminating the pathological response to neoadjuvant chemoradiotherapy in locally advanced rectal cancer. Sci Rep. 2017;7:8496.
29. Detsky JS, Keith J, Conklin J, Symons S, Myrehaug S, Sahgal A, Heyn CC, Soliman H. Differentiating radiation necrosis from tumor progression in brain metastases treated with stereotactic radiotherapy: utility of intravoxel incoherent motion perfusion MRI and correlation with histopathology. J Neurooncol. 2017;134: 433–441.
30. Ding Y, Hazle JD, Mohamed AS, Frank SJ, Hobbs BP, Colen RR, Gunn GB, Wang J, Kalpathy-Cramer J, Garden AS, Lai SY, Rosenthal DI, Fuller CD. Intravoxel incoherent motion imaging kinetics during chemoradiotherapy for human papillomavirus-associated squamous cell carcinoma of the oropharynx: preliminary results from a prospective pilot study. NMR Biomed. 2015;28: 1645–1654.
31. Paudyal R, OH JH, Riaz N, Venigalla P, Li J, Hatzoglou V, Leeman J, Nunez DA, Lu Y, Deasy JO, Lee N, Shukla-Dave A. Intravoxel incoherent motion diffusion-weighted MRI during chemoradiation therapy to characterize and monitor treatment response in human papillomavirus head and neck squamous cell carcinoma. J Magn Reson Imaging. 2017;45:1013–1023.
32. Le Bihan D. Intravoxel incoherent motion perfusion MR imaging: a wake-up call. Radiology. 2008;249:748–752.
33. Jensen JH, Helpern JA, Ramani A, Lu H, Kaczynski K. Diffusional kurtosis imaging: the quantification of non-gaussian water diffusion by means of magnetic resonance imaging. Magn Reson Med. 2005;53:1432–1440.
34. Jansen JF, Koutcher JA, Shukla-Dave A. Non-invasive imaging of angiogenesis in head and neck squamous cell carcinoma. Angiogenesis. 2010;13:149–160.
35. Jansen JF, Lu Y, Stambuk HE, Lee NY, Koutcher JA, Shukla-Dave A. Kurtosis analysis for DWI improves prediction of short-term response in head and neck cancer. Proc Int Soc Magn Reson Med 2011;1505.
36. Lu Y, Jansen JF, Mazaheri Y, Stambuk HE, Koutcher JA, Shukla-Dave A. Extension of the intravoxel incoherent motion model to non-gaussian diffusion in head and neck cancer. J Magn Reson Imaging. 2012;36:1088–1096.
37. Grieve SM, Blamire AM, Styles P. Elimination of Nyquist ghosting caused by read-out to phase-encode gradient cross-terms in EPI. Magnet Reson Med. 2002; 47:337–343.
38. Rasband WS. ImageJ. Bethesda, MD: U. S. National Institutes of Health; 1997–2016.
39. Ghossein R, Ganly I, Biagini A, Robenshtok E, Rivera M, Tuttle RM. Prognostic factors in papillary microcarcinoma with emphasis on histologic subtyping: a clinicopathologic study of 148 cases. Thyroid. 2014;24:245–253.
40. Ganly I, Ibrahimpasic T, Rivera M, Nixon I, Palmer F, Patel SG, Tuttle RM, Shah JP, Ghossein R. Prognostic implications of papillary thyroid carcinoma with tall-cell features. Thyroid. 2014;24:662–670.
41. Fluss R, Faraggi D, Reiser B. Estimation of the Youden Index and its associated cutoff point. Biom J. 2005;47:458–472.
42. Youden WJ. Index for rating diagnostic tests. Cancer. 1950;3:32–35.
43. RstudioTeam. RStudio: Integrated Development for R. Boston, MA: RStudio, Inc; 2015.
44. Stata Statistical Software: Release 15. College Station, TX: StataCorp LLC; 2017.

45. Rivera M, Ricarte J, Tuttle RM, Ganly I, Shaha A, Knauf J, Fagin J, Ghossein R. Molecular, morphologic, and outcome analysis of thyroid carcinomas according to degree of extrathyroid extension. Thyroid. 2010;20:1085–1093.
46. Hao Y, Pan C, Chen W, Li T, Zhu W, Qi J. Differentiation between malignant and benign thyroid nodules and stratification of papillary thyroid cancer with aggressive histological features: whole-lesion diffusion-weighted imaging histogram analysis. J Magn Reson Imaging. 2016;44:1546–1555.
47. Valerio M, Zini C, Fierro D, Giura F, Colarieti A, Giuliani A, Laghi A, Catalano C, Panebianco V. 3T multiparametric MRI of the prostate: does intravoxel incoherent motion diffusion imaging have a role in the detection and stratification of prostate cancer in the peripheral zone? Eur J Radiol. 2016;85:790–794.
48. Barbieri S, Bronnimann M, Boxler S, Vermathen P, Thoeny HC. Differentiation of prostate cancer lesions with high and with low Gleason score by diffusion-weighted MRI. Eur Radiol. 2017;27:1547–1555.
49. Shen J, Xu XQ, Su GY, Hu H, Shi HB, Liu W, Wu FY. Intravoxel incoherent motion magnetic resonance imaging of the normal-appearing parotid glands in patients with differentiated thyroid cancer after radioiodine therapy. Acta Radiol. 2018;59:204–211.
50. Becker AS, Wurnig MC, Finkenstaedt T, Boss A. Non-parametric intravoxel incoherent motion analysis of the thyroid gland. Heliyon. 2017;3:e00239.
51. Jansen JF, Stambuk HE, Koutcher JA, Shukla-Dave A. Non-gaussian analysis of diffusion-weighted MR imaging in head and neck squamous cell carcinoma: a feasibility study. AJNR Am J Neuroradiol. 2010;31:741–748.
52. Skare S, Newbould RD, Clayton DB, Albers GW, Nagle S, Bammer R. Clinical multishot DW-EPI through parallel imaging with considerations of susceptibility, motion, and noise. Magnet Reson Med. 2007;57:881–890.
53. Lu Y, Hatzoglou V, Banerjee S, Stambuk HE, Gonen M, Shankaranarayanan A, Mazaheri Y, Deasy JO, Shaha AR, Tuttle RM, Shukla-Dave A. Repeatability investigation of reduced field-of-view diffusion-weighted magnetic resonance imaging on thyroid glands. J Comput Assist Tomogr. 2015;39:334–339.